Nanotechnology **19** (2008) 025701 (12pp) doi:10.1088/0957-4484/19/02/025701

Electromechanical interactions in a carbon nanotube based thin film field emitting diode

N Sinha[1], D Roy Mahapatra[2], Y Sun[1], J T W Yeow[1], R V N Melnik[3] and D A Jaffray[4]

[1] Department of Systems Design Engineering, University of Waterloo, Waterloo, ON, N2L3G1, Canada
[2] Department of Aerospace Engineering, Indian Institute of Science, Bangalore 560012, India
[3] M2NeT Laboratory, Wilfrid Laurier University, Waterloo, ON, N2L3C5, Canada
[4] Department of Radiation Physics, Princess Margaret Hospital, Toronto, ON, M5G2M9, Canada

E-mail: jyeow@engmail.uwaterloo.ca

Received 13 September 2007
Published 6 December 2007
Online at stacks.iop.org/Nano/19/025701

Abstract

Carbon nanotubes (CNTs) have emerged as promising candidates for biomedical x-ray devices and other applications of field emission. CNTs grown/deposited in a thin film are used as cathodes for field emission. In spite of the good performance of such cathodes, the procedure to estimate the device current is not straightforward and the required insight towards design optimization is not well developed. In this paper, we report an analysis aided by a computational model and experiments by which the process of evolution and self-assembly (reorientation) of CNTs is characterized and the device current is estimated. The modeling approach involves two steps: (i) a phenomenological description of the degradation and fragmentation of CNTs and (ii) a mechanics based modeling of electromechanical interaction among CNTs during field emission. A computational scheme is developed by which the states of CNTs are updated in a time incremental manner. Finally, the device current is obtained by using the Fowler–Nordheim equation for field emission and by integrating the current density over computational cells. A detailed analysis of the results reveals the deflected shapes of the CNTs in an ensemble and the extent to which the initial state of geometry and orientation angles affect the device current. Experimental results confirm these effects.

(Some figures in this article are in colour only in the electronic version)

1. Introduction

Field emission from CNTs was first reported in 1995 by three research groups [1–3]. With significant improvement in processing techniques, applications of CNTs in field emission devices (e.g., field emission displays, x-ray tube sources, electron microscopes, cathode-ray lamps, nanolithography systems etc) have been successfully demonstrated [4–6]. The cathodes in these devices are better electron field emitters than Spindt-type emitters and diamond structures [7]. The field emission performance of a single isolated CNT is found to be remarkable, and this is due to structural integrity, high thermal conductivity, chemical stability and geometry of the CNTs. However, the situation becomes highly complex for cathodes comprising an ensemble of CNTs, where the individual CNTs are not always aligned normal to the substrate surface. Figure 1 shows an SEM image in which the CNT tips are oriented in a random manner. This is the most common situation, which can evolve from an initially ordered state of uniformly distributed and vertically oriented CNTs. Such an evolution process must be analyzed accurately from the viewpoint of long-term performance of the device. The authors' interests towards such an analysis and design studies stem from the problem of precision biomedical x-ray generation.

In this paper, we focus on a diode configuration, where the cathode contains a CNT thin film grown/deposited on a

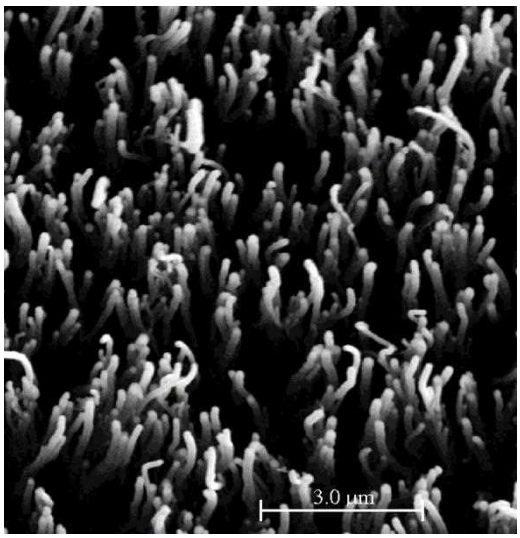

Figure 1. SEM image showing randomly oriented tips of CNTs in a thin film.

metallic substrate and the anode is a magnesium–aluminum alloy plate acting as emission current collector. Here, the most important requirement is to have a stable field emission current without compromising on the lifetime of the device. With the behavior of the CNT films remaining less predictable, the mechanisms responsible for CNT failures are also not clearly understood so far. Failure could be due to electromechanical deformation and stress, residual gases, ballistic transport induced impulse and partial discharge (PD) between cathode and anode. Several studies have reported experimental observations confirming the degradation and failure of CNT cathodes [8–11]. The degradation of a CNT thin film emitter is always gradual [11] but with several small-scale fluctuations and spikes. Such an overall gradual degradation occurs either during initial current–voltage measurement or during measurements under constant applied voltage over a long time duration.

To date, from mathematical modeling and design points of view, the detailed models and methods of system characterization are available only for vertically aligned CNTs grown on a patterned surface [12, 13]. In a CNT thin film, the array of CNTs may ideally be aligned vertically. However, in such a film, it is desired that the individual CNTs be evenly separated, so that their spacing is greater than their height to minimize the screening effect. Unfortunately, when the screening effect is minimized in this manner, the emission properties as well as the lifetimes of the cathodes are adversely affected due to a significant reduction in the density of CNTs. On the other hand, for a cathode with randomly oriented CNTs, the field emission current is produced by two types of source: (i) CNTs that point towards the current collector (anode) and (ii) oriented CNTs subjected to electromechanical forces causing reorientation. Therefore, a possible advantage of a cathode with randomly oriented CNTs is that a large number of CNTs always take part in the field emission over a longer time duration [7]. For this reason, a thin film with randomly oriented multi-walled carbon nanotubes (MWNTs) has been considered while formulating the mathematical model. From the modeling aspect, this becomes a general case, but is much more challenging compared to the case of a thin film with uniformly aligned CNTs. Although some preliminary works have been reported (see e.g., [14–16]), a much more detailed characterization needs to be done, especially in situations where the array of CNTs may undergo complicated dynamics during the process of charge transport. Also, in order to account for the randomly oriented CNTs and interaction among them, it is necessary to consider the space charge and the electromechanical forces responsible for their realignment. Some of the related factors are also important from device design considerations.

In this paper, the process of evolution, reorientation (self-assembly of CNTs) and electrodynamic interaction among the CNTs in the film, and the influence of these processes on the device output current are analyzed, based on a multiphysics model developed recently by the authors (see [16] for details). Here, first a homogeneous nucleation rate model is employed by considering a representative volume element (cell) to idealize the degradation and fragmentation of CNTs, phenomenologically. The film volume is discretized by several such cells across the planer dimensions of the film. A cell contains a specified number of CNTs with prescribed parametric shape distribution and a certain amount of carbon clusters as the initial description of the state. At a given time, the evolved concentration of carbon clusters due to the process of degradation and CNT fragmentation is obtained from the homogeneous nucleation rate model. This information is then used in a time-incremental manner to describe the evolved state of the CNTs in the cells. Finally, the field emission induced current density at the anode (cell-wise) is calculated by using the CNT tip orientation angles and the effective electric field in the Fowler–Nordheim equation. The diode current is then computed by integrating the cell-wise current density over the anode area. In this paper, while carrying out numerical simulations based on the above scheme, we focus on visualizing various details, e.g., the reorientation of the CNTs in the ensemble. From a system perspective, such a detailed study proves to be helpful in understanding the reason behind the experimentally observed fluctuation in the device current. To this end, we show experimental results and a quantitative comparison with simulations, confirming the reorientation and degradation of the CNTs.

2. Model formulation

2.1. Background

The physics of field emission from metallic surfaces is fairly well understood. The current density (J) due to field emission from a metallic surface is usually obtained by using the Fowler–Nordheim equation [17], which can be expressed as

$$J = \frac{BE^2}{\Phi} \exp\left(-\frac{C\Phi^{3/2}}{E}\right), \tag{1}$$

where E is the electric field, Φ is the work function for the cathode material, and B and C are constants. In the CNT

thin film problem, under the influence of sufficiently high voltage at ultra-high vacuum, the electrons emitted from the CNTs (mainly from the CNT tip region and emitted parallel to the axis of the tubes) reach the anode. Unlike metallic emitters, here, the surface of the cathode is not smooth. The cathode consists of CNTs (often in curved shapes) with certain spacings. In addition, a certain amount of impurities and carbon clusters may be present within the otherwise empty spaces in the film. Moreover, the CNTs undergo reorientation due to electromechanical interactions with the neighboring CNTs during field emission. This makes the determination of current density more difficult.

2.2. Mathematical model

We employ a homogeneous nucleation model to include the effect of degradation and CNT fragmentation, phenomenologically. This nucleation model is then coupled with a model of electromechanical interaction within the cell-wise ensemble of CNTs via the carbon cluster concentration. These two steps of our modeling approach are discussed in the following subsections.

2.2.1. Nucleation coupled model for degradation of CNTs. Let N_T be the total number of carbon atoms (in the CNTs and in the cluster form) in a representative volume element (V_{cell}) of the thin film, N be the number of CNTs in the cell, and N_{CNT} be the total number of carbon atoms present in a CNT. Hence,

$$N_T = NN_{CNT} + N_{cluster}, \tag{2}$$

where $N_{cluster}$ is the total number of carbon atoms in the cluster form in a cell at time t, and it is given by

$$N_{cluster} = V_{cell}\int_0^t \mathrm{d}n_1(t), \tag{3}$$

where n_1 is the concentration of carbon atoms in the cluster form in the cell. Therefore, by combining equations (2) and (3), one can obtain the number of CNTs in the cell as

$$N = \frac{1}{N_{CNT}}\left[N_T - V_{cell}\int_0^t \mathrm{d}n_1(t)\right]. \tag{4}$$

In order to determine $n_1(t)$, we introduce a homogeneous nucleation model [18, 19], which is to describe the evolution in $n_1(t)$. Here, we modify the original model (it was proposed in the context of an aerosol and a chemical growth process) by assuming the degradation as a reverse process of growth and model the phenomena of CNT degradation (the nucleation theory has been used for the growth of CNTs [20] and other nanoparticles [21, 22] also). Based on this modified model, the evolution equations are expressed as

$$\frac{\mathrm{d}N_{kin}}{\mathrm{d}t} = J_{kin}, \tag{5}$$

$$\frac{\mathrm{d}S}{\mathrm{d}t} = -\frac{J_{kin}Sg^*}{n_1} - (S-1)\frac{B_1A_n}{2v_1}, \tag{6}$$

$$\frac{\mathrm{d}M_1}{\mathrm{d}t} = J_{kin}d_p^* + (S-1)B_1N_{kin}, \tag{7}$$

$$\frac{\mathrm{d}A_n}{\mathrm{d}t} = \frac{J_{kin}Sg^{*2/3}s_1}{n_1} + \frac{2\pi B_1S(S-1)M_1}{n_1}, \tag{8}$$

where N_{kin} is the kinetic normalization constant, J_{kin} is the kinetic nucleation rate, S is the cluster saturation ratio, g^* is the critical cluster size, A_n is the total surface area of the cluster, v_1 is the monomer volume, M_1 is the moment of the cluster size distribution, d_p^* is the diameter of the particle of the critical cluster, and s_1 is the surface area of a monomer. In equations (5)–(8), the various other quantities involved are given by

$$S = \frac{n_1}{n_s}, \qquad M_1 = \int_{d_p^*}^{d_p^{max}} (n(d_p,t)d_p)\,\mathrm{d}(d_p), \tag{9}$$

$$N_{kin} = \frac{n_1}{S}\exp(\Theta), \qquad B_1 = 2n_sv_1\sqrt{\frac{kT}{2\pi m_1}}, \tag{10}$$

$$J_{kin} = \frac{\beta_{ij}n_1^2}{12S}\sqrt{\frac{\Theta}{2\pi}}\exp\left(\Theta - \frac{4\Theta^3}{27(\ln S)^2}\right), \tag{11}$$

$$g^* = \left(\frac{2}{3}\frac{\Theta}{\ln S}\right)^3, \qquad d_p^* = \frac{4\sigma v_1}{kT\ln S}, \tag{12}$$

where n_s is the equilibrium saturation monomer concentration, d_p is the cluster diameter, d_p^{max} is the maximum diameter of the clusters, $n(d_p, t)$ is the particle size distribution function, Θ is the dimensionless surface tension, k is Boltzmann's constant, T is the temperature, m_1 is the mass of monomer, β_{ij} is the collision frequency function for collisions between i-mers and j-mers, and σ is the surface tension. The collision frequency function (β_{ij}) is given by

$$\beta_{ij} = \left(\frac{3v_1}{4\pi}\right)^{1/6}\sqrt{\frac{6kT}{\rho_p}\left(\frac{1}{i}+\frac{1}{j}\right)}(i^{1/3}+j^{1/3})^2. \tag{13}$$

The dimensionless surface tension (Θ) is expressed as [18]

$$\Theta = \frac{\sigma s_1}{kT}, \tag{14}$$

where ρ_p is the particle mass density. In this paper, we have considered $i = 1$ and $j = 1$ for numerical simulations; that is, only monomer type clusters are considered. Our main intention in this context is to find n_1 using equation (5). However, during the growth of clusters, the change in the particle size (distribution) with time is governed by the saturation ratio (ratio of atomic concentration to the concentration at saturation). Therefore, equation (6) is required. In growth related kinetics, the growth is measured by the moment of cluster size distribution [23]. M_1 in equations (7) and (8) tells us about the distribution of the cluster size over time. That is, at different locations in the cell, different sizes of cluster can form, and that also affects how the equilibrium occurs. During growth of the clusters, a critical size nucleus is a cluster of size such that its rate of growth is equal to its rate of decay. The quantity A_n indicates the area of the stable carbon cluster. To know the area of the cluster, A_n is required. So, based on the established kinetic theory, we need to include all the four equations. For instance, in equation (8) for $\mathrm{d}A_n/\mathrm{d}t$, the

first term on the right-hand side of the equation describes an increase/decrease in the surface area due to a newly formed stable cluster and the second term means an increase in area of the existing stable cluster. Equations (5)–(8) form a set of four nonlinear coupled ordinary differential equations in $n_1(t)$, $S(t)$, $M_1(t)$ and $A_n(t)$. This system of equations is solved with the help of a finite difference scheme. Finally, the average number of CNTs in a cell, and hence the average height distribution with a known number of CNTs in the ensemble, are obtained with the help of equation (4).

2.2.2. Effects of CNT geometry and orientation. As discussed in section 1, the geometry and the orientation of CNTs play important roles in the field emission performance of the film and hence must be considered in the model. In section 2.2.1, a model of degradation and fragmentation of CNTs has been formulated. Following this model, if Δh is the decrease in the length of the CNT over a time interval Δt due to degradation and if d_t is the diameter of the CNT, then the surface area of the CNT decreases by $\pi d_t \Delta h$. By using the geometry of the CNT, the decreased surface area can be expressed as

$$\pi d_t \Delta h = V_{\text{cell}} n_1(t)[s(s-a_1)(s-a_2)(s-a_3)]^{1/2}, \quad (15)$$

where a_1, a_2, a_3 are lattice constants, and $s = \frac{1}{2}(a_1 + a_2 + a_3)$. The chiral vector for the CNT is expressed as

$$\vec{C}_h = n\vec{a}_1 + m\vec{a}_2, \quad (16)$$

where n and m are integers ($n \geqslant |m| \geqslant 0$) and the pair (n, m) defines the chirality of the CNT. By using the fact that $\vec{a}_1 \cdot \vec{a}_1 = |a_1|^2$, $\vec{a}_2 \cdot \vec{a}_2 = |a_2|^2$, and $2\vec{a}_1 \cdot \vec{a}_2 = |a_1|^2 + |a_2|^2 - |a_3|^2$, the circumference and the diameter of the CNT can be expressed as [24], respectively,

$$|\vec{C}_h| = \sqrt{n^2 a_1^2 + m^2 a_2^2 + nm(a_1^2 + a_2^2 - a_3^2)}, \qquad d_t = \frac{|\vec{C}_h|}{\pi}. \quad (17)$$

By defining the rate of degradation of CNT as $v_{\text{burn}} = \lim_{\Delta t \to 0} \Delta h / \Delta t$, and by dividing both sides of equation (15) by Δt, one has

$$\pi d_t v_{\text{burn}} = V_{\text{cell}} \frac{\mathrm{d}n_1(t)}{\mathrm{d}t}[s(s-a_1)(s-a_2)(s-a_3)]^{1/2}. \quad (18)$$

By combining equations (17) and (18), v_{burn} can be simplified as

$$v_{\text{burn}} = V_{\text{cell}} \frac{\mathrm{d}n_1(t)}{\mathrm{d}t}\left[\frac{s(s-a_1)(s-a_2)(s-a_3)}{n^2 a_1^2 + m^2 a_2^2 + nm(a_1^2 + a_2^2 - a_3^2)}\right]^{1/2}. \quad (19)$$

Next, we calculate the effective electric field at a given time step. The electric field at the deflected tip (see figure 2) is approximated as

$$E_{z'} = \sqrt{1 - \frac{x^2 + y^2}{R^2}} \frac{(\text{Present height})}{(\text{Present gap})} E_0, \quad (20)$$

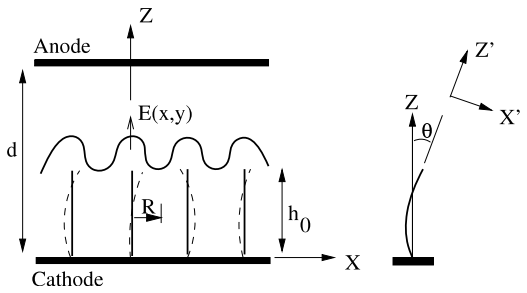

Figure 2. CNT array configuration.

where x and y are the deflections of the tip with respect to its original location, $2R$ is the spacing between two adjacent CNTs at the cathode substrate, and $E_0 = V/d$ with V as the applied DC voltage. As the CNTs degrade, their height also decreases with time. On the other hand, the distance between the tip and the anode increases with time due to reduction in the height of the CNTs. With the above assumption, the present height of the CNT can be written as $h_0 - v_{\text{burn}}t$, and hence the present distance between the tip and the anode can be expressed as $d - h_0 + v_{\text{burn}}t$. Here, h_0 is the initial average height of the CNTs and d is the distance between the cathode substrate and the anode (see in figure 2). Equation (20) can now be rewritten as

$$E_{z'} = \sqrt{1 - \frac{x^2 + y^2}{R^2}} \frac{(h_0 - v_{\text{burn}}t)E_0}{(d - h_0 + v_{\text{burn}}t)}. \quad (21)$$

Subsequently, the effective electric field, which is required for field emission calculation, can be expressed as

$$E_z = E_{z'} \cos\theta(t), \quad (22)$$

where $\theta(t)$ is the tip orientation angle that a CNT makes with the Z-axis, as shown in figure 2. The current density is calculated by substituting the value of E_z in the Fowler–Nordheim equation. The above formulation takes into account the effect of CNT tip orientations, and one can perform a statistical analysis of the device current for randomly distributed and randomly oriented CNTs. However, due to the deformation of the CNTs under electromechanical forces, the evolution process requires a much more detailed treatment. In order to account for the changing orientations, we estimate the effects of electromechanical forces as discussed next.

2.2.3. Electromechanical forces. For each CNT, the orientation angle θ is dependent on the electromechanical forces. Based on the studies reported in the literature, it is reasonable to expect that a major contribution is by the Lorentz force due to the flow of electron gas along the CNT and the ponderomotive force due to electrons in an oscillatory electric field. In addition, the electrostatic force and the van der Waals force are also important.

The components of the Lorentz force along the Z- and X-directions (see figure 2) are approximated as

$$f_{lz} = \pi d_t e\hat{n} E_{1z}, \qquad f_{lx} = \pi d_t e\hat{n} E_{1x} \approx 0, \quad (23)$$

where e is the electronic charge (positive), $\hat{n}$ is the surface electron density and E_{1z} is the fluctuating electric field due to electron flow in the CNTs. We now decompose the surface electron density into a steady (unstrained) part and a fluctuating part; that is,

$$\hat{n} = \hat{n}_0 + \hat{n}_1, \tag{24}$$

where the steady part $\hat{n}_0$ corresponds to the Fermi level energy in an unstrained CNT, and it can be approximated as [25]

$$\hat{n}_0 = \frac{kT}{\pi b^2 \Delta}, \tag{25}$$

where b is the interatomic distance and Δ is the overlap integral ($\approx$2 eV for carbon). In equation (24), the fluctuating part $\hat{n}_1$ is inhomogeneous along the length of the CNTs. Actually, $\hat{n}_1$ should be coupled nonlinearly with the deformation and the electromagnetic field [26]. However, in a simplified form, $\hat{n}_1$ is primarily governed by the quantum-hydrodynamic continuity equation:

$$\dot{\hat{n}}_1 + \hat{n}_0 \frac{\partial \dot{u}_{z'}}{\partial z'} = 0, \tag{26}$$

with $u_{z'}$ as the longitudinal displacement, and we employ this simplified equation to compute $\hat{n}_1$ at a given time step. In equation (23), the fluctuating electric field $\mathbf{E}_1 = (E_{1x}, E_{1z})$ is computed using a Green's function approach as discussed in [27].

The ponderomotive force, which acts on free charges on the surface of CNTs under oscillatory high field, tends to straighten the bent CNTs in the Z-direction. Furthermore, the ponderomotive forces induced by the applied electric field stretch every CNT [28]. In order to estimate the components of the ponderomotive force (f_{p_x}, f_{p_z}) acting on the tip region (see [29]), the following approximations are used:

$$f_{p_z} \approx \frac{q^2}{2m_e\omega^2} E_{1z} \frac{\partial E_{1z}}{\partial z}, \qquad f_{p_x} \approx 0, \tag{27}$$

where $q = (\pi d_t e\hat{n})\,\mathrm{d}s$ is the total charge on an elemental segment $\mathrm{d}s$ of a CNT, m_e is the mass of an electron, $\omega = 2\pi/\tau$, τ is the relaxation frequency, and f_{p_z} is the Z-component of the ponderomotive force. The X-component of the ponderomotive force f_{p_x} is assumed to be negligible.

In order to calculate the electrostatic force, interactions among the neighboring CNTs are considered. Let us assume two small segments of two neighboring CNTs of lengths $\mathrm{d}s_1$ and $\mathrm{d}s_2$, respectively. The charges on these two segments are given by, respectively,

$$q_1 = e\hat{n}(\pi d_t^{(1)})\,\mathrm{d}s_1, \qquad q_2 = e\hat{n}(\pi d_t^{(2)})\,\mathrm{d}s_2, \tag{28}$$

where $d_t^{(1)}$ and $d_t^{(2)}$ are the diameters of two neighboring CNTs (1) and (2), respectively. The electrostatic force on the segment $\mathrm{d}s_1$ by the segment $\mathrm{d}s_2$ is given by

$$\frac{1}{4\pi\epsilon\epsilon_0}\frac{q_1 q_2}{r_{12}^2},$$

where $\epsilon\epsilon_0$ denotes the effective permittivity of the aggregate of CNTs and carbon clusters and r_{12} is the effective distance between the centroids of the segments $\mathrm{d}s_1$ and $\mathrm{d}s_2$. The force on the segment $\mathrm{d}s_1$ of one CNT due to the entire segment (s_2) of the neighboring CNT can be expressed as

$$\frac{1}{4\pi\epsilon\epsilon_0}\int_0^{s_2} \frac{1}{r_{12}^2}(e\hat{n}\pi d_t^{(1)}\,\mathrm{d}s_1 e\hat{n}\pi d_t^{(2)})\,\mathrm{d}s_2.$$

Therefore, the force per unit length on s_1 due to s_2 is

$$f_c = \frac{1}{4\pi\epsilon\epsilon_0}\int_0^{s_2} \frac{(\pi e\hat{n})^2 d_t^{(1)} d_t^{(2)}}{r_{12}^2}\,\mathrm{d}s_2. \tag{29}$$

The differential of the force $\mathrm{d}f_c$ acts along the line joining the centroids of the segments ds_1 and ds_2. Therefore, the components of the force f_c in the X-direction and the Z-direction are, respectively,

$$\begin{aligned} f_{c_x} &= \int \mathrm{d}f_c \cos\phi = \frac{1}{4\pi\epsilon\epsilon_0}\int_0^{s_2} \frac{(\pi e\hat{n})^2 d_t^{(1)} d_t^{(2)}}{r_{12}^2}\cos\phi\,\mathrm{d}s_2 \\ &\equiv \frac{1}{4\pi\epsilon\epsilon_0}\sum_{j=1}^{h_0/\Delta s_2} \frac{(\pi e\hat{n})^2 d_t^{(1)} d_t^{(2)}}{r_{12}^2}\cos\phi\,\Delta s_2, \end{aligned} \tag{30}$$

$$\begin{aligned} f_{c_z} &= \int \mathrm{d}f_c \sin\phi = \frac{1}{4\pi\epsilon\epsilon_0}\int_0^{s_2} \frac{(\pi e\hat{n})^2 d_t^{(1)} d_t^{(2)}}{r_{12}^2}\sin\phi\,\mathrm{d}s_2 \\ &\equiv \frac{1}{4\pi\epsilon\epsilon_0}\sum_{j=1}^{h_0/\Delta s_2} \frac{(\pi e\hat{n})^2 d_t^{(1)} d_t^{(2)}}{r_{12}^2}\sin\phi\,\Delta s_2. \end{aligned} \tag{31}$$

Here, ϕ is the angle that the force vector $\mathrm{d}\vec{f}_c$ makes with the X-axis, j is the node number, and Δs_2 is the length of discretized segments (assumed uniform in the present study). The effective distance (r_{12}) between the centroids of the segments $\mathrm{d}s_1$ and $\mathrm{d}s_2$ is obtained as

$$r_{12} = [(d_1 - l_{x_2} + l_{x_1})^2 + (l_{z_1} - l_{z_2})^2]^{1/2}, \tag{32}$$

where d_1 is the spacing between the CNTs while in contact with the surface of the cathode substrate, and l_{x_1} and l_{x_2} are the deflections of the segments of two neighboring CNTs (relative deflection considering the two end nodes of each of the segments), respectively, which are parallel to the X-axis. Similarly, l_{z_1} and l_{z_2} are the deflections of the two segments which are parallel to the Z-axis.

Next, we consider the van der Waals effect. The van der Waals force plays important roles, not only in the interaction of the CNTs with the substrate, but also in the interaction between the walls of MWNTs and CNT bundles. Under bending type deformation, the cylindrical symmetry of the CNTs is no longer preserved, leading to axial–radial coupling [30]. For simplicity, let us restrict ourselves to a two-dimensional (2D) situation described with respect to the (X, Z) coordinate system shown in figure 2, and let us assume that the lateral and longitudinal displacements of a CNT are $u_{x'}$ and $u_{z'}$, respectively. Due to their large aspect ratio, it is reasonable to idealize the CNTs as one-dimensional elastic members (as in an Euler–Bernoulli beam [31]). Therefore, the kinematics can be expressed as

$$u_{z'}^{(m)} = u_{z'0}^{(m)} - r^{(m)}\frac{\partial u_{x'}^{(m)}}{\partial z'}, \tag{33}$$

where the superscript (m) indicates the mth wall of the MWNT with $r^{(m)}$ as its radius and $u_{z'0}$ as the displacement of the center of the cylindrical cross-section. Under tension, bending moment and shear force, the longitudinal displacement of the cross-section of one wall relative to the cross-section of its neighboring wall can be expressed with the help of equation (33) as

$$\Delta_{z'}^{(m)} = u_{z'}^{(m+1)} - u_{z'}^{(m)} = r^{(m+1)}\frac{\partial u_{x'}^{(m+1)}}{\partial z'} - r^{(m)}\frac{\partial u_{x'}^{(m)}}{\partial z'}, \quad (34)$$

where we assume $u_{x'}^{(m)} = u_{x'}^{(m+1)} = \Delta_{x'}$ as the lateral displacement due to pressure in the thin film device. The lateral shear stress $\tau_{\mathrm{vs}}^{(m)}$ due to the van der Waals effect can be written as

$$\tau_{\mathrm{vs}}^{(m)} = C_{\mathrm{vs}}\frac{\Delta_{z'}^{(m)}}{\Delta_{x'}}, \quad (35)$$

where C_{vs} is the van der Waals coefficient. Therefore, the effective shear force per unit length of CNT can be expressed as

$$f_{\mathrm{vs}} = \sum_m \int_0^{2\pi} C_{\mathrm{vs}}\frac{\Delta_{z'}^{(m)}}{\Delta_{x'}}\left(\frac{r^{(m+1)} + r^{(m)}}{2}\right)\mathrm{d}\psi,$$

$$\Rightarrow f_{\mathrm{vs}} = \sum_m \pi C_{\mathrm{vs}}[(r^{(m+1)})^2 - (r^{(m)})^2]\frac{1}{\Delta_{x'}}\frac{\partial \Delta_{x'}}{\partial z'}. \quad (36)$$

The components of the van der Waals force parallel to the Z- and the X-directions are, respectively,

$$f_{\mathrm{vs}_z} = f_{\mathrm{vs}}\sin\theta(t), \qquad f_{\mathrm{vs}_x} = f_{\mathrm{vs}}\cos\theta(t). \quad (37)$$

2.2.4. Modeling the reorientation of CNTs. The net force components acting on the CNTs parallel to the Z- and X-directions can now be calculated as

$$f_z = \int (f_{lz} + f_{\mathrm{vs}_z})\,\mathrm{d}s + f_{\mathrm{c}_z} + f_{p_z}, \quad (38)$$

$$f_x = \int (f_{lx} + f_{\mathrm{vs}_x})\,\mathrm{d}s + f_{\mathrm{c}_x} + f_{p_x}. \quad (39)$$

Next, we employ these force components in the expression of work done on the ensemble of CNTs and formulate an energy conservation law (see, e.g., [31]).

Under the assumption of small strain and small curvature, the longitudinal strain ε_{zz} (including thermal strain) and stress σ_{zz} can be written as, respectively,

$$\varepsilon_{zz} = \frac{\partial u_{z'0}^{(m)}}{\partial z'} - r^{(m)}\frac{\partial^2 u_{x'}^{(m)}}{\partial z'^2} + \alpha\Delta T(z'), \qquad \sigma_{zz} = E'\varepsilon_{zz}, \quad (40)$$

where E' is the effective modulus of elasticity of CNTs under consideration, $\Delta T(z') = T(z') - T_0$ is the difference between the absolute temperature (T) during field emission and a reference temperature (T_0), and α is the effective coefficient of thermal expansion (longitudinal). The longitudinal strain and stress from equation (40) are employed in the strain energy expression. Subsequently, the kinetic energy is expressed in terms of the velocities $\dot{u}_{x'}$ and $\dot{u}_{z'}$. Next, by applying Hamilton's principle, we obtain the governing equations in $(u_{x'},\ u_{z'})$ for each CNT, which can be expressed as, respectively,

$$E'A_2\frac{\partial^4 u_{x'}^{(m)}}{\partial z'^4} + \rho A_0\ddot{u}_{x'}^{(m)} - \rho A_2\frac{\partial^2 \ddot{u}_{x'}^{(m)}}{\partial z'^2} - \sum_m \pi C_{\mathrm{vs}}[(r^{(m+1)})^2 - (r^{(m)})^2]\frac{1}{\Delta_{x'}}\frac{\partial \Delta_{x'}}{\partial z'}\cos\left(\theta(z')\right) - f_{lx'} - f_{cx'} = 0, \quad (41)$$

$$-E'A_0\frac{\partial^2 u_{z'0}^{(m)}}{\partial z'^2} - \frac{1}{2}E'A_0\alpha\frac{\partial \Delta T(z')}{\partial z'} + \rho A_0\ddot{u}_{z'0}^{(m)} - \pi C_{\mathrm{vs}}[(r^{(m+1)})^2 - (r^{(m)})^2]\frac{1}{\Delta_{x'}}\frac{\partial \Delta_{x'}}{\partial z'}\sin\left(\theta(z')\right) - f_{lz'} - f_{cz'} = 0, \quad (42)$$

where A_0 is the effective cross-sectional area, A_2 is the second moment of cross-sectional area about the Z-axis and ρ is the mass per unit length of CNT. We assume a fixed boundary condition $(u = 0)$ at the substrate–CNT interface $(z = 0)$ and a forced boundary condition at the CNT tip $(z = h(t))$.

2.2.5. Effects of temperature. In order to arrive at the governing equation in temperature $T(z')$, the process of heating of CNTs during field emission is idealized as follows. During field emission, an electron flowing from the cathode substrate towards the anode along the CNT surface acquires energy and escapes from the tip region towards the anode by crossing the Fermi energy. The energy lost in the replacement of the emitted electron is assumed to create an intense temperature gradient in the emitter [32]. By neglecting the radiation of heat, the resistive heating of CNTs, together with the usual laws of heat conduction, leads to the following differential equation:

$$(h - z')^4\frac{\partial^2 T}{\partial z'^2} + 2(h - z')^3\frac{\partial T}{\partial z'} - \bar{\alpha}^2(h - z')^4\dot{T} = \bar{b}\dot{T}^2, \quad (43)$$

where

$$\bar{b} = \frac{-I^2\rho_c}{4\pi^2(4.18\kappa)(1 - \cos\upsilon_0)^2}, \qquad \bar{\alpha}^2 = \frac{\bar{\rho}C}{\kappa}, \quad (44)$$

where I is the time varying current, ρ_c is the electrical resistivity, κ is the thermal conductivity, υ_0 is the interior half angle of the CNT tip, $\bar{\rho}$ is the mass density, and C is the specific heat (see [32] for details). We assume the temperature boundary condition, that at $z = h$, if $|\theta| \leqslant \theta_{\mathrm{c}}$ then $T(t) = T_{\mathrm{c}}$ else $T(t) = T(t_i) = T(t_{i-1})$, and $\dot{T} = 0$ for all time; that is, the temperature at the tip of a CNT has a constant value T_{c} when that tip is oriented within a prescribed range $[-\theta_{\mathrm{c}}, +\theta_{\mathrm{c}}]$. For tip orientations $|\theta| > \theta_{\mathrm{c}}$, the temperature is tracked over time steps $(\Delta t = t_i - t_{i-1})$ based on the solution of the initial boundary value problem governed by equations (41)–(43).

Each CNT is discretized into a number of segments with length Δs. As in the finite element method, each of these segments has two end nodes where the variables $u_{x'}$, $u_{z'}$ and T are evaluated. At each time step, the governing equations (41)–(43) are solved and the curved shape $s(x' + u_{x'}, z' + u_{z'})$ of each of the CNTs is updated. The angle of orientation θ between the

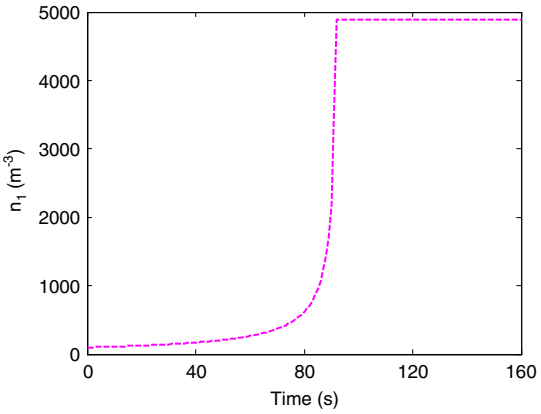

Figure 3. Variation of the carbon cluster concentration with time. Initial condition: $n_1(0) = 100$, $S(0) = 5000$, $M_1(0) = 2.12 \times 10^{-16}$, $A_n(0) = 0$.

nodes $j+1$ and j at the two ends of segment Δs_j is expressed as

$$\theta(t) = \tan^{-1}\left(\frac{(x^{j+1} + u_x^{j+1}) - (x^j + u_x^j)}{(z^{j+1} + u_z^{j+1}) - (z^j + u_z^j)}\right), \tag{45}$$

$$\begin{bmatrix} u_x^j \\ u_z^j \end{bmatrix} = [\Gamma(\theta(t - \Delta t)^j)] \begin{bmatrix} u_{x'}^j \\ u_{z'}^j \end{bmatrix}, \tag{46}$$

where Γ is the usual coordinate transformation matrix which maps the displacements $(u_{x'}, u_{z'})$ defined in the local (X', Z') coordinate system into the displacements (u_x, u_z) defined in the cell coordinate system (X, Z). For this transformation, we employ the angle $\theta(t - \Delta t)$ obtained at the previous time step and for each node $j = 1, 2, 3, \ldots$.

3. Results and discussions

The computational scheme involves three parts: (i) discretization of the nucleation coupled model for degradation of CNTs, (ii) incremental update of the CNT geometry using the electromechanical forces, and (iii) calculation of the field emission current. At $t = 0$, the CNTs are assumed to be oriented randomly. This random distribution is parameterized in terms of the upper bound of the CNT tip deflection which is given by $\Delta x_{\max} = h/m'$; $m' \gg 1$ is an integer. The angles are used to calculate the component of electromechanical forces. In the successive time step $t \leftarrow t + \Delta t$, the deformed state of the CNTs is computed and the tip angle of each CNT is updated.

The CNT film considered for a representative numerical simulation here consists of randomly oriented MWNTs. The film has a surface area (projected on the anode) of 49.93 mm^2 and average thickness of 10–14 μm. Actual experiments were performed on various films of both types, random as well as aligned CNTs. The films were placed in a pressure-control chamber fitted with a micrometer to control the electrode gap, and by connecting the diode to a resistive–capacitive circuit. Current histories were measured under a constant DC voltage for a controlled gap. In the simulation and analysis reported next, we have chosen the range of DC voltage and parameters related to the CNT distribution in the film as in the actual experimental set-up.

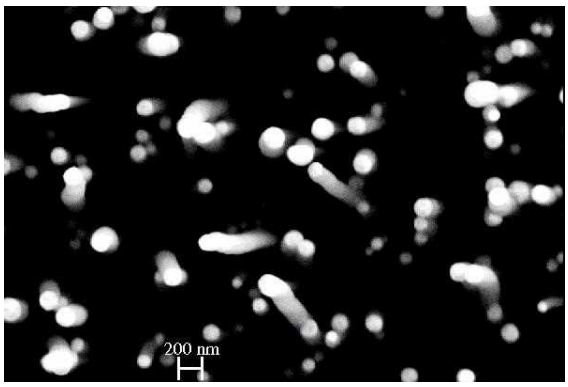

Figure 4. CNT tip distribution showing the area coverage under the anode. The area shown is approximately 5.08 μm × 5.08 μm.

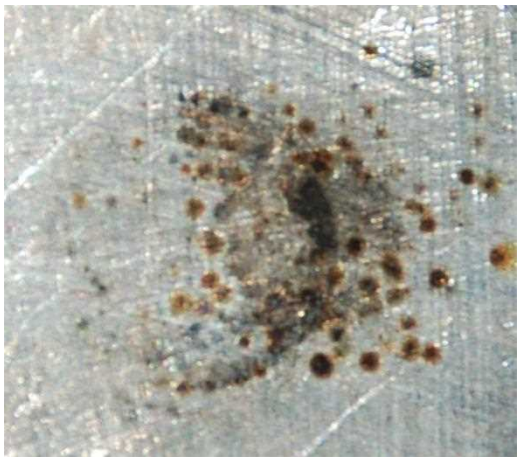

Figure 5. Dark spots on the anode after field emission showing the traces of clusters ejected from the CNT tips. Largest spot diameter ≈0.7 mm.

3.1. Degradation of CNT thin films

We have assumed that at $t = 0$, the diode contains a minimal amount of carbon clusters. The CNTs degrade over time (due to both fragmentation and self-assembly) and the carbon cluster concentration in each cell also changes (mostly increases) accordingly. Based on this assumption, the initial conditions were set as $n_1(0) = 100$, $S(0) = 5000$, $M_1(0) = 2.12 \times 10^{-16}$, $A_n(0) = 0$, and $T = T_0 = 303$ K. Figure 3 shows the $n_1(t)$ history over a small time interval of 160 s. Such evolution indicates that the carbon cluster concentration increases exponentially at the beginning and tends to a steady state afterwards at ≈93 s, indicating a saturation. Therefore, figure 3 indicates the time that the degradation process takes to reach saturation ($S(0) = 5000$) in the present analysis. Assuming that saturation has taken place within the computational cell, and assuming that this is the case for all the cells encompassing the entire volume between the cathode substrate and the anode, one can estimate $N_{\text{cluster}} = 5000 \times (0.049\,93)^2 \times 14 \times 10^{-6}$. Here, the film area

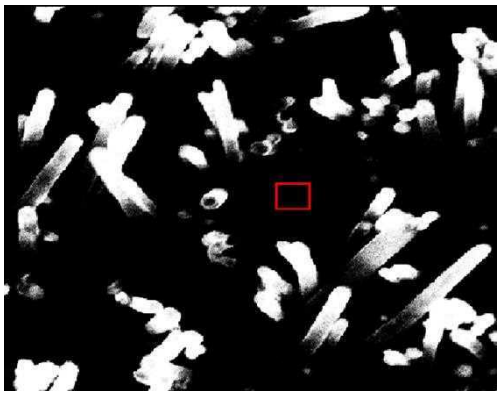

(a)

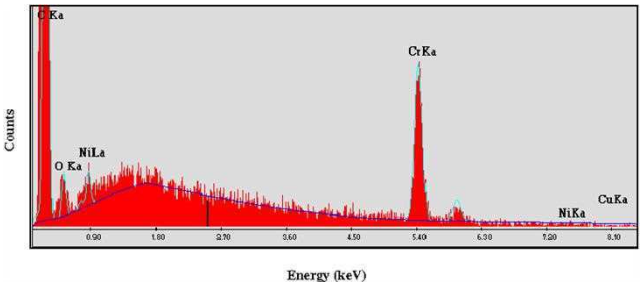

(b)

Figure 6. EDS results showing the exposed substrate surface made of Cr and Cu after the field emission. The energy spectrum shown in (b) corresponds to the region marked in (a).

(a)

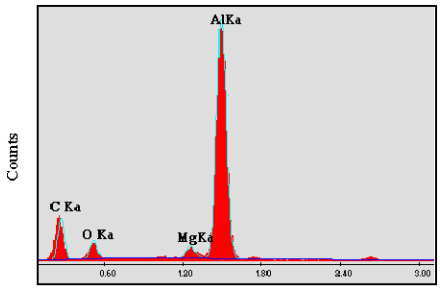

(b)

Figure 7. EDS results showing the deposited carbon clusters one the anode after field emission. The energy spectrum shown in (b) corresponds to the region marked in (a). Optical images of the spots are shown in figure 5.

is 49.93 mm^2 (as stated earlier) and the cathode to anode gap is assumed to be 14 μm (a less conservative estimate since the free space above the CNT film is excluded). From figure 4, we obtain the effective area projected on the anode for the degradation process to be approximately 10×10^{-4} times the total film area. Multiplying this factor to the number of clusters above, we estimate $N_{\text{cluster}} \approx 3.495 \times 10^{-10}$. The clusters assumed to be formed in this way are partly deposited on the cathode and partly pulled up ballistically and deposited on the anode. Results are discussed next.

Our experiments have revealed that degradation of CNTs into clusters is indeed one of the important processes that takes place during field emission. Interestingly, dark spots on the originally polished surface of the anode were found after 10 h of field emission from a vertically aligned CNTs. The spots were visible by the naked eye. Figure 5 shows an optical image of these spots. The spot diameters are found to be in the range 0.4–0.7 mm. The thin film substrate is made of CuCr alloy. In order to find out if there is any degradation of CNTs with any trace of exposed metal substrate and any trace of carbon clusters on the anode, we perform energy-dispersive x-ray spectroscopy (EDS) on the film and on the anode surface.

The EDS results in figure 6 shown for one of the sample substrate after 10 h of field emission indicates that the carbon clusters and the CNTs at various places were pulled up and the substrate was exposed. Along with Ni impurities, which are present due to catalytic processing of the CNTs, the spectral peaks of Cr can be clearly seen in figure 6. On the other hand, traces of carbon cluster are observed on the anode surface

Table 1. Trace of particles and their concentrations obtained from EDS measurements.

Emitter region	Element	Wt%	At.%
Cathode	C K	87.20	96.25
	O K	0.84	0.70
	CrK	11.96	3.05
	NiK	0.00	0.00
	CuK	0.00	0.00
Anode	C K	32.47	45.84
	O K	29.11	30.86
	MgK	1.11	0.77
	AlK	31.14	19.57
	ClK	6.18	2.96

(as shown in figure 5). EDS results reveal that the anode surface contains carbon, as indicated by the spectral peaks in figure 7. We quantify the possible nature of degradation process as follows. With the area of the anode exposed to x-rays corresponding to an $\approx$100 μm effective diameter spot (assumed to be smaller than the actual diameter observed, which is diffused) containing 45.04 at.% amorphous carbon (see table 1), we get $N_{\text{cluster}} \approx 3.353 \times 10^{-9}$. Comparing this estimate with the previously simulated value of 3.495×10^{-10} from the degradation model, it is reasonable to assume that the reorientation of the CNT tips actually activates or deactivates the degradation process differently in different cells and at different times. As a result, one may observe a much slower

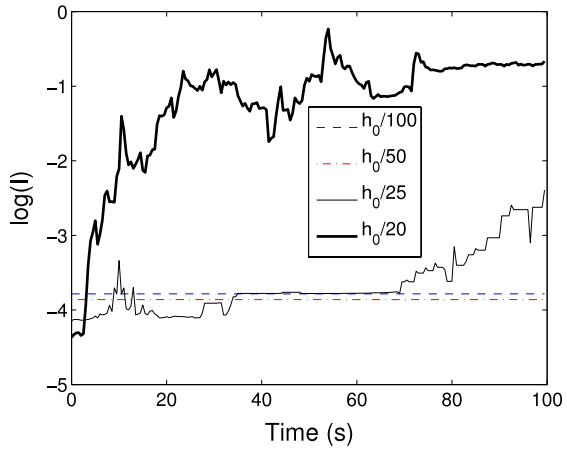

Figure 8. Simulated current histories for various uniform heights, uniform radius and uniform spacing of CNTs under a DC voltage of 600 V. The current I is in ampere units.

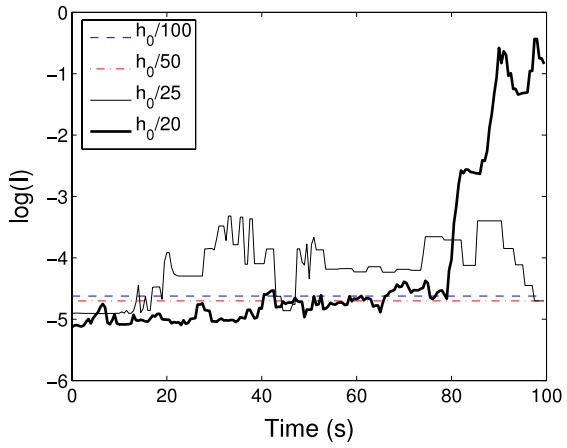

Figure 9. Simulated current histories for various nonuniform heights, uniform radius and uniform spacing of CNTs under a DC voltage of 600 V. The current I is in ampere units.

degradation in the ensemble. However, at present, it is not possible to observe the occurrence of the spots on the anode in a time-resolved manner.

The results analyzed above establish the fact that the degradation of CNTs is an important process. The influence of such degradation, along with the electromechanical forces, is expected to play a significant role on the device current. Next, we report the experimental results of field emission current fluctuation and analyze such behavior based on the proposed model and by comparing the simulations with the experimental data.

3.2. Device current

Here, we analyze the field emission current histories for $V = 600$ V. The constants B and C in equation (1) were taken as $B = (1.4 \times 10^{-6}) \times \exp((9.8929) \times \Phi^{-1/2})$ and $C = 6.5 \times 10^{7}$, respectively [33]. It has been reported in the literature (see, e.g., [33]) that the work function Φ for CNTs is smaller than the work functions for metal, silicon and graphite. However, depending on the types of CNTs (i.e., SWNT/MWNT), there are significant variations in the experimentally estimated values of Φ, geometric parameters and also the type of substrate materials having significant influence on the electronic band-edge potential. Here, simulations have been carried out based on $\Phi = 2.2$ eV.

The following two cases are considered for numerical simulations: (i) average height between neighboring CNTs in the film sample $h_0 = 12$ μm, uniform radius $r = 2.75$ nm and uniform spacing $d_1 = 2$ μm, and (ii) a random initial height distribution: $h = (h_0 \pm 2\ \mu\text{m}) \mp 2\ \mu\text{m} \times \text{rand}(1)$, uniform radius and uniform spacing. Here the function rand denotes random number generator. The electrode gap (d) is maintained at 34.7 μm. Several computational runs are performed and the output data are averaged out at each sampling time step. The current histories for cases (i) and (ii) are shown in figures 8, and 9, respectively. The four curves in figures 8 and 9 correspond to four different initial states with increasing values: $\Delta x_{\max} = h_0/100$, $h_0/50$, $h_0/25$, and $h_0/20$. Interestingly, both these figures tell us the following: (1) as the initial state of deflections/angle increases (from $h_0/100$ to $h/50$ and higher), the average current reduces, until h_0/m' becomes large enough that during field emission, the electrodynamic interaction among CNTs produces a sudden

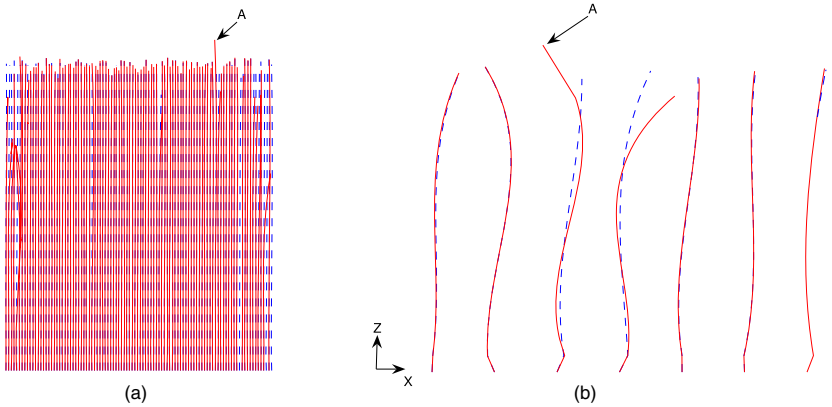

Figure 10. (a) Array of 100 CNTs (nonuniform height distribution with maximum initial tip deflections of $h_0/20$); (b) enlarged view of the region near the pulled up CNT (marked as 'A' and deflected horizontally ≈ 2 μm). The initial shape is shown by the dashed line and the deflected shapes at $t = 100$ s are shown by solid lines.

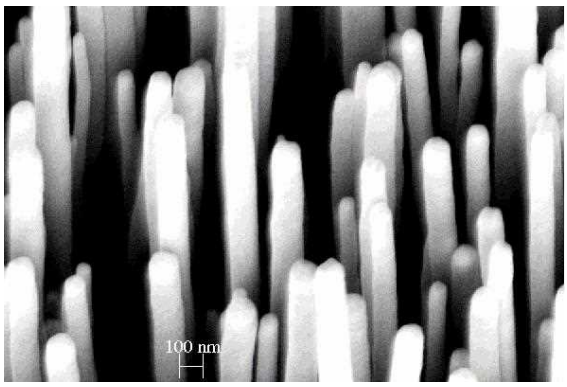

Figure 11. Vertically aligned CNTs before field emission.

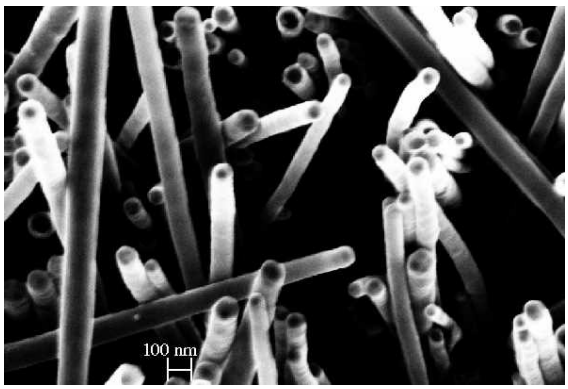

Figure 13. Reoriented CNTs after 10 h of field emission.

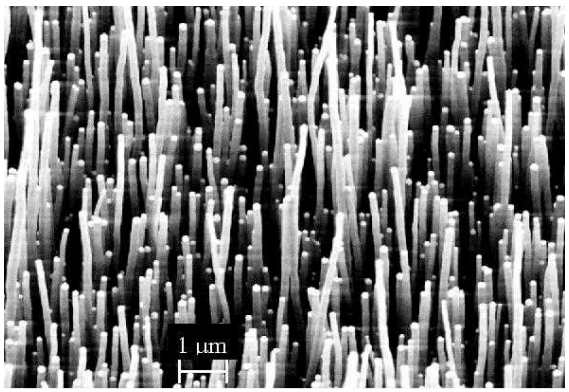

Figure 12. Small reorientations and electrodynamic force induced stretching of CNTs before long duration exposure.

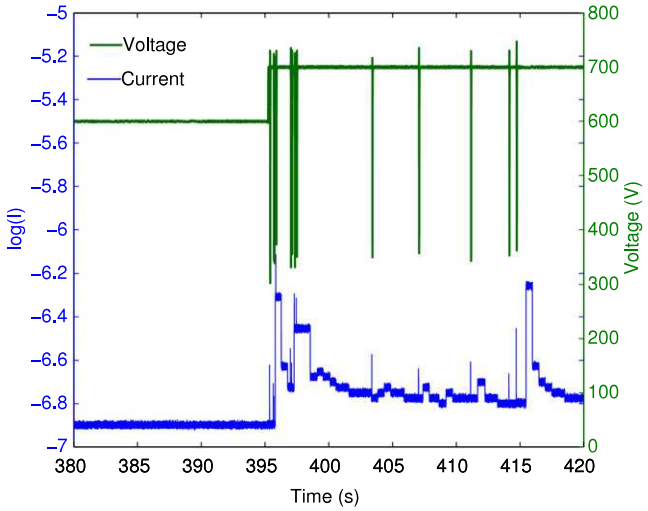

Figure 14. Fluctuation of field emission current from a baked sample having vertically aligned CNTs.

pull in the deflected tips towards the anode (see the CNT tip marked as 'A' in figure 10 and deflected horizontally ≈2 μm) resulting in transients (sometimes current >mA, as can be seen from the $h_0/20$ curve); (2) the trends in the current fluctuation for higher h_0/m' in figure 8 compared to figure 9 prove that the nonuniform distribution of height (h) gives better stabilized current for large random orientations. Also, in this case of nonuniform height distribution in figure 9, as one goes from $h_0/25$ to $h_0/20$ curves, the trend in the average current level is more uniform than in the uniform height case (see the $h_0/20$ curve in figure 8, which rises >100 mA at the very beginning, which is undesired in x-ray device applications). On the other hand, the above results also support the earlier reported experimental observation that a thin film with randomly oriented CNTs produces larger current density compared to a thin film with uniformly aligned CNTs. The above results also justify several experimental observations, which have been reported in the literature from a comparative perspective of using a single CNT and then different types of CNT in thin films and the effect of their alignments [4, 8, 34–36]. For example, Collins and Zettl [34] attribute the change in currents to interactions between neighboring CNTs.

In the field emission experiments, we have exposed several experimental samples having randomly oriented as well as vertically aligned CNTs. Figure 11 shows the SEM image of one such sample having vertically aligned CNTs. In figure 12, the SEM image of the sample after a short period of exposure is shown. Figure 13 shows the SEM of the same sample as in figure 11 but after 10 h of field emission at 600 V. As seen in the simulated responses in figures 8 and 9, the spikes in the current are significant. This experimental results confirm a strong electromechanical interaction among the CNTs along with certain amount of degradations. The results shown in figure 14 are for an electrode gap of 150 μm. Occasional shortings of the electrical circuit were observed for smaller gaps between the electrodes. Such a short circuit condition is the result of pull up of one or more CNTs under the increased electrodynamic force.

Most interesting is figure 13 compared to figures 12 and 11. While figure 12 depicts small reorientations and electromechanical force induced stretching of CNTs for a short-term exposure, figure 13 clearly shows a combined effect of reorientations and degradation of a few CNTs (pulling up and exposing the substrate, as discussed earlier) after 10 h of field emission. With these experimental results, the proposed modeling framework and the simulated results regarding CNT tip deflections in figure 10 proves to be an important insight towards understanding the nature of the

field emission response. The results in figure 10 are also in agreement with a previously reported study [37]. Based on the simulations performed, the stress on the CNTs under a voltage of 700 V was estimated using equation (40). The maximum stress was found to be less than 20 GPa, which is generally much below the stress at fracture (65–93 GPa) [38].

4. Concluding remarks

In this paper, we have developed a modeling approach to analyze the evolution of CNT thin films and the effect of such evolution on the device current. A computational scheme has been implemented, which combines a homogeneous nucleation model of degradation and CNT fragmentation with successive electromechanical forcing. Numerical simulations based on this model and the computational scheme are able to capture the transients in the field emission current as observed in the actual experiments. Our analysis shows how the electromechanical interaction among the CNTs influences the orientation of individual CNTs in an ensemble, and consequently, how the distribution of CNTs and geometrical factors affect the device current. With this new finding reported in this paper, there are two important aspects which require further attention: one is the physics of the CNT fragmentation process under high field to explain the long time response of the device, and the other is the process of electron gas flow and ballistic transport under realistic geometric conditions.

References

[1] Rinzler A G, Hafner J H, Nikolaev P, Lou L, Kim S G, Tomanek D, Colbert D and Smalley R E 1995 Unraveling nanotubes: field emission from an atomic wire *Science* **269** 1550–3

[2] de Heer W A, Chatelain A and Ugrate D 1995 A carbon nanotube field-emission electron source *Science* **270** 1179–80

[3] Chernozatonskii L A, Gulyaev Y V, Kosakovskaya Z Y, Sinitsyn N I, Torgashov G V, Zakharchenko Y F, Fedorov E A and Valchuk V P 1995 Electron field emission from nanofilament carbon films *Chem. Phys. Lett.* **233** 63–8

[4] Bonard J M, Salvetat J P, Stockli T, Forro L and Chatelain A 1999 Field emission from carbon nanotubes: perspectives for applications and clues to the emission mechanism *Appl. Phys.* A **69** 245–54

[5] Saito Y and Uemura S 2000 Field emission from carbon nanotubes and its application to electron sources *Carbon* **38** 169–82

[6] Sugie H, Tanemure M, Filip V, Iwata K, Takahashi K and Okuyama F 2001 Carbon nanotubes as electron source in an x-ray tube *Appl. Phys. Lett.* **78** 2578–80

[7] Cheng Y and Zhou O 2003 Electron field emission from carbon nanotubes *C. R. Physique* **4** 1021–33

[8] Bonard J M, Maier F, Stockli T, Chatelain A, de Heer W A, Salvetat J P and Forro L 1998 Field emission properties of multiwalled carbon nanotubes *Ultramicroscopy* **73** 7–15

[9] Avouris P, Martel R, Ikeda H, Hersam M, Shea H R and Rochefort A 2000 Electrical properties of carbon nanotubes: spectroscopy, localization and electrical breakdown *Funda. Mat. Res. Series: Sci. Appl. Nanotubes* ed D Tomanek and R J Enbody (New York: Kluwer Academic/Plenum Publishers) pp 223–37

[10] Nilsson L, Groening O, Groening P and Schlapbach L 2001 Collective emission degradation behavior of carbon nanotube thin-film electron emitters *Appl. Phys. Lett.* **79** 1036–8

[11] Bonard J M, Klinke C, Dean K A and Coll B F 2003 Degradation and failure of carbon nanotube field emitters *Phys. Rev.* B **67** 115406

[12] Nicolaescu D, Filip L D, Kanemaru S and Itoh J 2004 Modeling of optimized field emission nanotriodes with aligned carbon nanotubes of variable heights *Japan. J. Appl. Phys.* **43** 485–91

[13] Nicolaescu D, Filip V, Kanemaru S and Itoh J 2003 Modeling of field emission nanotriodes with carbon nanotube emitters *J. Vac. Sci. Technol.* **21** 366–74

[14] Sinha N, Roy Mahapatra D, Yeow J T W, Melnik R V N and Jaffray D A 2006 Characterization of self-assembly and evolution in carbon nanotube thin film field emitter *Proc. 6th IEEE Conf. Nanotech. (Cincinnati, July 2006)*

[15] Sinha N, Roy Mahapatra D, Yeow J T W, Melnik R V N and Jaffray D A 2006 A coupled model of field emission from carbon nanotube thin films *Proc. 7th World Cong. Comp. Mech. (Los Angeles, July 2006)*

[16] Sinha N, Roy Mahapatra D, Yeow J T W, Melnik R V N and Jaffray D A 2007 Carbon nanotube thin film field emitting diode: understanding the system response based on multiphysics modelling *J. Comput. Theor. Nanosci.* **4** 535–49

[17] Fowler R H and Nordheim L 1928 Electron emission in intense electric field *Proc. R. Soc. Lond.* A **119** 173–81

[18] Friedlander S K 1983 Dynamics of aerosol formation by chemical reactions *Ann. New York Acad. Sci.* **404** 354–64

[19] Grishick S L, Chiu C P and McMurry P H 1990 Time-dependent aerosol models and homogeneous nucleation rates *Aerosol Sci. Technol.* **13** 465–77

[20] Watanabe T, Notoya T, Ishigaki T, Kuwano H, Tanaka H and Moriyoshi Y 2006 Growth mechanism for carbon nanotubes in a plasma evaporation process *Thin Solid Films* **506/507** 263–7

[21] Watanabe T and Fujiwara K 2004 Nucleation and growth of oxide nanoparticles prepared by induction thermal plasmas *Chem. Eng. Comm.* **191** 1343–61

[22] Watanabe T and Okumiya H 2004 Formation mechanism of silicide nanoparticles by induction thermal plasmas *Sci. Technol. Adv. Mater.* **5** 639–46

[23] Farrell J E and Valls O T 1991 Growth kinetics and domain morphology after off-critical quenches in a two-dimensional fluid model *Phys. Rev.* B **43** 630–40

[24] Jiang H, Zhang P, Liu B, Huang Y, Geubelle P H, Gao H and Hwang K C 2003 The effect of nanotube radius on the constitutive model for carbon nanotubes *Comput. Mater. Sci.* **28** 429–42

[25] Slepyan G Y, Maksimenko S A, Lakhtakia A, Yevtushenko O and Gusakov A V 1999 Electrodynamics of carbon nanotubes: dynamic conductivity, impedance boundary conditions, and surface wave propagation *Phys. Rev.* B **60** 17136–49

[26] Wei L and Wang Y-N 2004 Electromagnetic wave propagation in single-wall carbon nanotubes *Phys. Lett.* A **333** 303–9

[27] Svizhenko A, Anantram M P and Govindan T R 2005 Ballistic transport and electrostatics in metallic carbon nanotubes *IEEE Trans. Nanotechnol.* **4** 557–62

[28] Glukhova O E, Zhbanov A I, Torgashov I G, Sinistyn N I and Torgashov G V 2003 Ponderomotive forces effect on the field emission of carbon nanotube films *Appl. Surf. Sci.* **215** 149–59

[29] Musatov A L, Kiselev N A, Zakharov D N, Kukovitskii E F, Zhbanov A I, Izrael'yants K R and Chirkova E G 2001 Field electron emission from nanotube carbon layers grown by CVD process *Appl. Surf. Sci.* **183** 111–9

[30] Ruoff R S, Tersoff J, Lorents D C, Subramoney S and Chan B 1993 Radial deformation of carbon nanotubes by van der Waals forces *Nature* **364** 514–6

[31] Reddy J N 2002 *Energy Principles and Variational Methods in Applied Mechanics* (New Jersey: Wiley)
[32] Dolan W W, Dyke W P and Trolan J K 1953 The field emission initiated vacuum arc II. the resistively heated emitter *Phys. Rev.* **91** 1054–7
[33] Huang Z P, Tu Y, Carnahan D L and Ren Z F 2004 Field emission of carbon nanotubes *Encyl. Nanosci. Nanotechnol.* vol 4, ed H S Nalwa (Stevenson Ranch: American Scientific Publishers) pp 401–16
[34] Collins P G and Zettl A 1997 Unique characteristics of cold cathode carbon nanotube matrix field emitters *Phys. Rev.* B **55** 9391–9
[35] Chen Y, Shaw D T and Guo L 2000 Field emission of different oriented carbon nanotubes *Appl. Phys. Lett.* **76** 2469–71
[36] Kuttel O M, Groening O, Emmeneger C and Schlapbach L 1998 Electron field emission from phase pure nanotube films grown in a methane/hydrogen plasma *Appl. Phys. Lett.* **73** 2113–5
[37] Zhbanov A I and Glukhova O E 2001 Lengthening of nanotubes in strong electrical fields *Proc. 14th Int. Microelect. Conf.* pp 63–4
[38] Belytschko T, Xiao S P, Schatz G C and Ruoff R S 2002 Atomistic simulations of nanotube fracture *Phys. Rev.* B **65** 235430